Influence of blade deflections on wind turbine noise directivity

Bresciani, A. P.C.; Boatto, U.; Le Bras, S.; Bonnet, P.; De Santana, L. D.

DOI
10.1088/1742-6596/2257/1/012012

Publication date
2022

Document Version
Final published version

Published in
Journal of Physics: Conference Series

Influence of blade deflections on wind turbine noise directivity

Influence of blade deflections on wind turbine noise directivity

A P C Bresciani[1,2,3], U Boatto[4,5], S Le Bras[1], P Bonnet[4] and L D de Santana[2]

[1]Siemens Industry Software N.V., Interleuvenlaan 68, Leuven, 3001, Belgium
[2]University of Twente, PO Box 217, Enschede, 7500 AE, the Netherlands.
[3]Centre Scientifique et Technique du Bâtiment (CSTB), 24, rue Joseph Fourier, 38400, Saint Martin d'Hères, France
[4]Siemens Industry Software N.V., Rue des Chasseurs Ardennais 8, Angleur, 4031, Belgium.
[5]Delft University of Technology, Department of Aerodynamic Wind Energy and Propulsion, Kluyverweg 1, 2629 HS, Delft, the Netherlands.

E-mail: a.p.c.bresciani@utwente.nl

Abstract. This paper establishes the effect of blade deflections on wind turbine noise directivity. Fast turn-around methods are used in a framework of integrated aeroelastic and aeroacoustic simulations: the blade element momentum theory is coupled with a RANS-informed Amiet's model for the aeroacoustic modelling of trailing- and leading-edge noise. This approach is applied to the NREL 5 MW wind turbine and the results of rigid and flexible blades are compared. The overall sound pressure level computed with flexible blades increases up to 13 dBA for listeners close to the rotor plane. This effect is attributed to the flapwise angular deflection of the wind turbine blade. Furthermore, the symmetry of the results with respect to the rotor plane is lost when the flapwise deflection is considered, indicating that the modelling of this rotation is of fundamental importance for the acoustic simulation.

1. Introduction

Large blades installed in modern horizontal axis wind turbines experience significant deflections within the operating life. Recent simulations reproducing the rated power production conditions predicted axial deflections ranging from 8 to 9% of the rotor radius for a 5 MW-class turbine [1,2], around 10% for a 10 MW-class [3], and significantly more than 10% for a 15 MW-class wind turbine [4].

Few studies established the relation between the rotor aeroelasticity and changes on the wind turbine noise emissions. This relation is of particular interest in view of the known extent of deflections for modern large wind turbines. The effect of blade deflections on acoustic results has been studied by Kim et al. [5] with a vortex lattice method, non-linear composite beam theory and semi-empirical models for the noise sources. However, the change in the noise directivity has not been addressed in much detail. Kaviani and Nejat [6] performed Detached Eddy Simulation (DES) coupled with a finite element method to model the blade deformation of a 70 m diameter, 1.5 MW wind turbine. Only a single point spectrum computed with Ffowcs-Williams and Hawkings (FW-H) technique has been provided, giving little insight into the acoustics effect of flexible blades.

In the present work the effect of the blade deflections on the noise directivity is studied considering the NREL 5 MW wind turbine [7]. This 126-meter diameter wind turbine is representative of modern onshore wind turbines. For wind turbines in design operating conditions, trailing-edge noise has been recognised as the most important noise contribution [8]. In this work the leading-edge noise contribution is also considered, highlighting under which conditions it becomes the dominant noise source. Semi-analytical and semi-empirical aeroelastic and aeroacoustic prediction methods are chosen to investigate several operating conditions and to compare the noise radiated by flexible and rigid blades. They are based on the Blade Element Momentum Theory (BEMT) and Amiet's theory [9, 10]. The use of semi-analytical and semi-empirical models has some limitations since these models rely on simplifying assumptions and are calibrated against experimental data which can lead to poor prediction for other flow conditions or blade profiles, e.g., attached blade flow, thin airfoils, inviscid wake flow. However, they lead to fast numerical simulations compared to high-fidelity methods, e.g., direct noise computation or DES coupled with FW-H as in reference [6], which provide accurate results but are often too computationally expensive to be applied to industrial geometries and different operating conditions. In this study a Reynolds Averaged Navier–Stokes (RANS)-informed Amiet's theory investigated by [11, 12] for 2D airfoils and wind turbines is applied to the NREL 5 MW wind turbine. An extension of the methodology is proposed to account for the blade deformation effects.

The numerical method used to compute wind turbine noise accounting for blade deformation is presented in section 2. In section 3, the Blade Element Momentum Theory (BEMT), the RANS approach and the Amiet's model are validated for the NREL 5 MW wind turbine. The aeroacoustic results are reported in section 4. The conclusions of this paper are summarised in section 5.

2. Methodology

A diagram of the methodology adopted in this study is shown in fig. 1. For the acoustic simulation, the 3D CAD of the blade is divided into segments in the spanwise direction using Simcenter 3D software [13]. For each segment, the mid-span airfoil is used in a 2D RANS simulation necessary to compute the boundary layer parameters for the trailing-edge noise Amiet's theory. The blade segments have a constant aspect ratio $\lambda = L_{\text{span}}/c_{\text{mean}}$, where L_{span} is the spanwise extension of the segment and c_{mean} is the chord length of the airfoil in the middle of the segment. Since, in general, the blade cannot be exactly divided into segments with constant λ, the segment closer to the root is enlarged up to the first cross-section of the blade with an airfoil shape. For the NREL turbine hereby considered, the blade is divided in 5 segments: the 4 outer segments have a constant aspect ratio $\lambda = 3$, while the one closer to the root has $\lambda = 4.5$ to include the blade up to $R = 11.75$ m, where the first airfoil-shaped cross-section is located. The part comprised between the rotor centre and $R = 11.75$ m has been neglected for the acoustic simulation because the circular cross-section is not suited for the application of Amiet's theory. Furthermore, the inner part of the blade is known to have a small contribution the noise due to its low velocity [14]. The value $\lambda \geq 3$ is chosen to satisfy the large aspect ratio assumption required by the formulation of Amiet's theory used in the present work. The BEMT is used for the aeroelastic simulations and detailed in section 2.1. The real angle of attack including the pitchwise deflection and the induced angle of attack are linearly interpolated at the radial positions defined for the acoustic simulations and used for the 2D RANS simulations. The pitchwise and flapwise deflections are used to compute the free-field noise directivity with Amiet's theory. For the flapwise deflection, the blade displacement is neglected and only the rotation of the blade section is considered.

The methodology described above can be applied with an arbitrary wind speed profile to simulate the atmospheric boundary layer: the rotor disk must be discretized also in the azimuthal

direction to account for the varying wind speeds and a 2D RANS simulation should be performed for each azimuthal position and blade segment. In the present work, the wind speed is supposed to be uniform over the rotor disk to obtain axisymmetric conditions and, so, drastically reduce the number of 2D RANS simulations necessary. As shown by Tian and Cotté [15], the modelling of the wind shear has negligible effects on the trailing-edge noise, which, as shown in section 4, is the main noise source up to the rated conditions. For this reason, the conclusions of the present work are not expected to change if the effect of the wind shear is included.

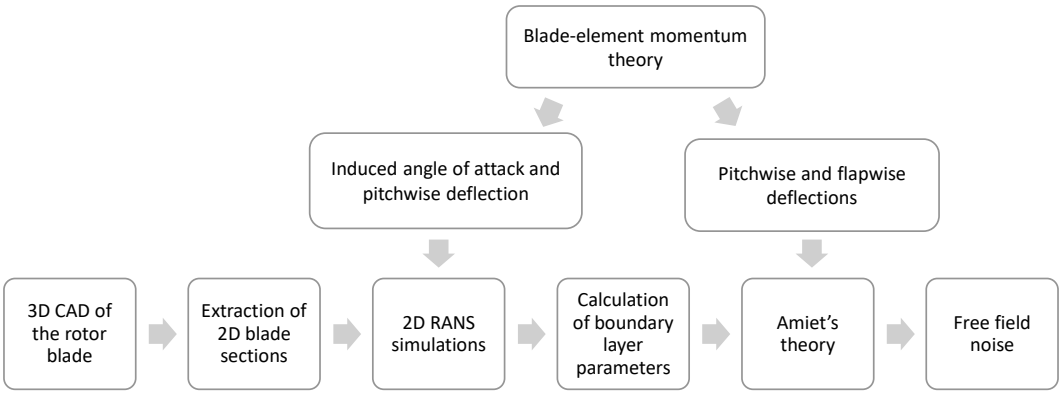

Figure 1: Diagram of the numerical workflow

2.1. Blade element momentum theory

In this study, a flexible multi-body simulation is performed with the Simcenter Samcef Mecano [16] software. The solver combines a finite element discretization of the Timoshenko beam theory for large displacements and rotations with the non-linear multi-body framework. This approach is suited to the simulation of vibrating flexible structures within mechanisms subject to complex loads, such as wind turbine blades [17]. The blade aerodynamic forces are computed by a BEMT-based load element that includes all the state-of-the-art engineering corrections employed in similar wind turbine aero-servo-elastic industrial codes [18, 19]. In the present study, the employed BEMT solution consists of the quasi-static Glauert's BEMT theory [20] corrected by the Burton's version [21] of the Prandlt tip and root loss factor [22] and the Buhl's turbulent wake state correction [23].

2.2. RANS-informed Amiet's theory

Amiet [9, 10] developed a semi-analytical theory to predict leading- and trailing-edge airfoil noise. The extension of this model to rotating blades is due to Schlinker and Amiet [24] and it is known in literature as strip theory: the blade is divided in strips to account for the different relative velocities and Amiet's theory for leading- and trailing-edge noises is applied to each strip. This model has been successfully applied to predict the noise generated from different types of rotors, such as fans [25–29], helicopters [24] and wind turbines [12,15,30,31]. In Amiet's theory, the airfoil is modelled as an infinitely thin flat plate with chord $c = 2b$, span $L = 2d$ and at zero angle of attack with respect to the freestream velocity U. If the observer is located in the acoustic and geometrical far-field and the aspect ratio L/c of the flat plate is large, the power spectral density for trailing-edge noise S_{pp}^{TE} is computed as [32]:

$$S_{pp}^{TE}(\mathbf{x},\omega) = \left(\frac{\omega x_3 b}{2\pi c_0 \sigma_0^2}\right)^2 4d|\mathcal{I}(x_1,k_{10},k_{20})|^2 l_y(k_{10},k_{20})\Phi_{pp}(k_{10},k_{20}), \quad (1)$$

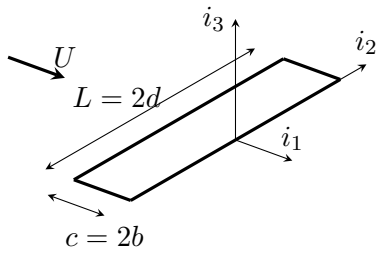

Figure 2: Reference frame for trailing-edge noise.

where $\mathbf{x} = (x_1, x_2, x_3)$ is the position of the observer in the reference frame depicted in fig. 2; ω is the pulsation; c_0 is the speed of sound; $\sigma_0 = \sqrt{x_1^2 + \beta^2(x_2^2 + x_3^2)}$; $\mathcal{I} = \mathcal{I}_1 + \mathcal{I}_2$ is the aeroacoustic transfer function for trailing-edge noise, given in [32, 33]; $k_{10} = \omega/U_c$ with $U_c = 0.7U$; $k_{20} = kx_2/\sigma_0$ with $k = \omega/c_0$; l_y is the spanwise correlation length obtained from Corcos model [34]; Φ_{pp} is the wall pressure spectrum computed with empirical models for computational efficiency.

Empirical [35–38] and analytical models [39] for the wall pressure spectrum have been proposed in literature. However, they need as input boundary layer parameters extracted at the trailing-edge, such as the boundary layer thickness, the wall shear stress, the maximum shear stress and the pressure gradient. All these parameters can be extracted from 2D RANS simulations, allowing a trade-off between low computational cost and accuracy. In the present work, Lee's model [37] has been applied in case of adverse pressure gradient, while Goody's [35] has been used for zero or negative pressure gradient. The extraction location is at 99% of the chord on both sides of the airfoil. To apply Amiet's theory, the blade segments are linearized in flat plates. Their orientation in space is defined by two angles: the pitch angle and the cone angle. The pitch is given by the sum of the twist, the collective pitch and the torsional deformation; the cone is computed using the cone angle of the rotor (set to 0 in this work) and the flapwise deflection angle.

The 2D RANS simulations are performed with CFD software STAR-CCM+ [40]. The turbulence model k-ω SST is used and all the simulations are wall-resolved, i.e. with $y^+ < 1$. The γ-transition model [41] is used to model the laminar-to-turbulent flow transition. All the RANS simulation setup, including the meshing process and the computation of the boundary layer parameters, is fully automated in STAR-CCM+.

Amiet's formulation for leading-edge noise reads

$$S_{pp}^{LE}(\mathbf{x}, \omega) = \left(\frac{\rho\omega c x_3}{2c_0\sigma_0^2}\right)^2 \pi U d |\mathcal{L}(x_1, k_{10}, k_{20})|^2 \Phi_{ww}(k_{10}, k_{20}), \tag{2}$$

where ρ is the air density, $\mathcal{L} = \mathcal{L}_1 + \mathcal{L}_2$ is the aeroacoustic transfer function for leading-edge noise [33] and Φ_{ww} is the inflow turbulence spectrum modelled using the von Karman spectrum in this work. The inputs required by the von Karman spectrum are the wind turbulence intensity and integral length scale. Both quantities depend on the location of the wind turbine, the surrounding environment and the time of the day. Since experimental data for comparison are not available, an integral length scale of 120 m and a turbulence intensity of 10% have been chosen as values representative for typical operating conditions [42, 43].

The pitchwise and flapwise deflections are considered as additional rotation matrices for each blade segment. For the pitchwise deflection, the additional pitch angle resulting from the torsion of the blade is used; for the flapwise deflection, the angle considered is comprised between the deformed blade span axis and the rotor plane. It is worth mentioning that, in the acoustic simulation, the displacement in the off-plane direction has been neglected. The noise

contributions from each airfoil are averaged in the azimuthal direction following [44] and, finally, summed.

3. Validation

The NREL 5 MW turbine is modelled as an untilted, unconed, isolated rotor similarly as in [2] and by employing the specifications provided in [7]. The 3D blade CAD geometry is generated by a Siemens Samtech and Universidad Nacional del Litoral in-house code using the aeroelastic simulation parameters and airfoil shapes given in reference [7].

Five conditions representative of steady-state power production operations are considered in this study. The operating conditions are shown in table 1 and the turbine is simulated with fully-rigid and fully-flexible blades, leading to a total of 10 simulations. Rigid blades are obtained by introducing rigid bodies into the blade finite element model to achieve zero deflections. The operational conditions are taken from [7] except for the pitch angle of the above-rated case which was modified to obtain a power value as close as possible to the predicted flexible rated power in table 2. Finally, the air density is set to 1.225 kg/m^3 and the speed of sound to 343.0 m/s.

Table 1: Simulation conditions employed in this study for both rigid and flexible blades.

Condition	Wind speed [m/s]	Rotor speed [rpm]	Pitch angle [°]
Below-rated	5.0	7.51	0.0
Below-rated	8.0	9.30	0.0
Below-rated	10.0	11.25	0.0
Rated	11.4	12.10	0.0
Above-rated	14.0	12.10	8.13

3.1. BEMT validation

The aeroelastic performance of the NREL 5 MW isolated rotor is first compared with the reference 3D unsteady RANS simulations performed by Dose et al. [2] for both rigid and flexible blades cases. First, the rotor thrust and power are compared in table 2 at rated conditions. BEMT can predict very well both quantities with an error below 1% in both simulation cases. For the flexible case, the aeroelastic code predicts 5.54 m axial blade tip deflection towards downwind and 0.62 m blade tip tangential deflection along the clockwise rotation direction according to an upwind observer. For both deflections, the mismatch with the reference is below 2%.

In fig. 3, the angles describing the flapwise ψ and pitchwise θ blade deflection components are shown for the five flexible cases. Both quantities reach their largest values in the outboard blade, as expected for rotor blades. The flapwise angle increases with wind speed until rated power where its largest value is achieved due to the largest thrust at that condition, as reported

Table 2: Comparison between thrust (Thr) and power (Pow) for the BEMT-based aeroelastic code and the reference results [2] for both rigid and flexible rotor cases at rated conditions.

Case	BEMT Thr	Ref. Thr	Δ Thr	BEMT Pow	Ref. Pow	Δ Pow
Rigid	759.1 kN	761.7 kN	-0.3%	5.56 MW	5.51 MW	0.9%
Flexible	765.3 kN	771.3 kN	-0.8%	5.54 MW	5.49 MW	0.9%

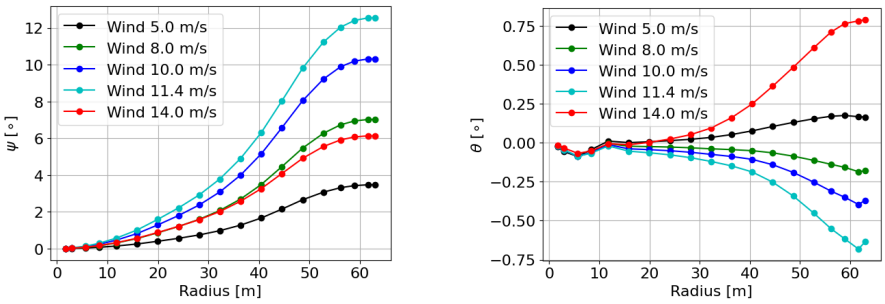

(a) (b)

Figure 3: Angles associated to the (a) flapwise and (b) pitchwise blade deflections predicted by the BEMT code for the simulation cases in table 2.

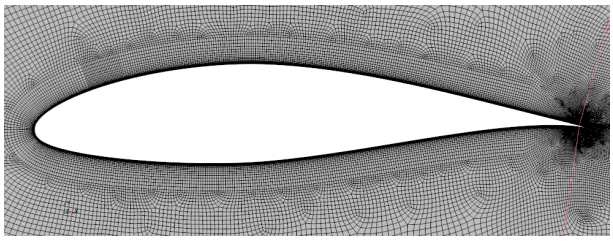

Figure 4: Mesh used for the tip segment airfoil. The pink lines at the trailing-edge correspond to the extraction locations for the boundary layer parameters.

in [7]. The torsion angle follows a similar trend (except for the 5m/s case) and the predicted negative values are related to a "nose-up" rotation of the airfoil section (i.e. opposite to positive aerodynamic twist angle) and increasing the local angle of attack, consistently with Dose's fluid-structure interaction simulations [2].

Finally, the blade structure was also validated by modal analysis of an isolated blade. The frequencies of the first three modes were compared with those reported in [2] obtaining less than 3% difference.

3.2. RANS validation

The five airfoils extracted from the five blade segments share the same set-up for the 2D RANS simulations. The computational domain has the typical C-shape used for airfoil analysis. The velocity inlet boundary condition is imposed in a semi-circumference located 25 chord-unit upstream of the leading-edge of the airfoil. The same boundary condition is imposed at the upper and lower boundaries. The outlet boundary is located 50 chord-unit downstream and a pressure outlet boundary condition is imposed to the same boundary.

The mesh is generated using the automatic quadrilateral mesher of STAR-CCM+. The structured inflation layer is composed by 40 cells in the wall-normal direction, ensuring a thickness of the first cell near the wall of $y^+ \approx 0.3$ and a smooth cell-size transition between the last cell of the inflation layer and the outer unstructured mesh. The resulting mesh for the airfoil used for the tip segment of the blade is shown in fig. 4. Each mesh counts approximately 67 000 elements.

A mesh convergence study has been performed with two additional meshes for each blade segment: a coarser mesh with 47 000 elements and a finer one with 107 000 elements. Both of them have been obtained with a uniform refinement/coarseness of the medium mesh. In

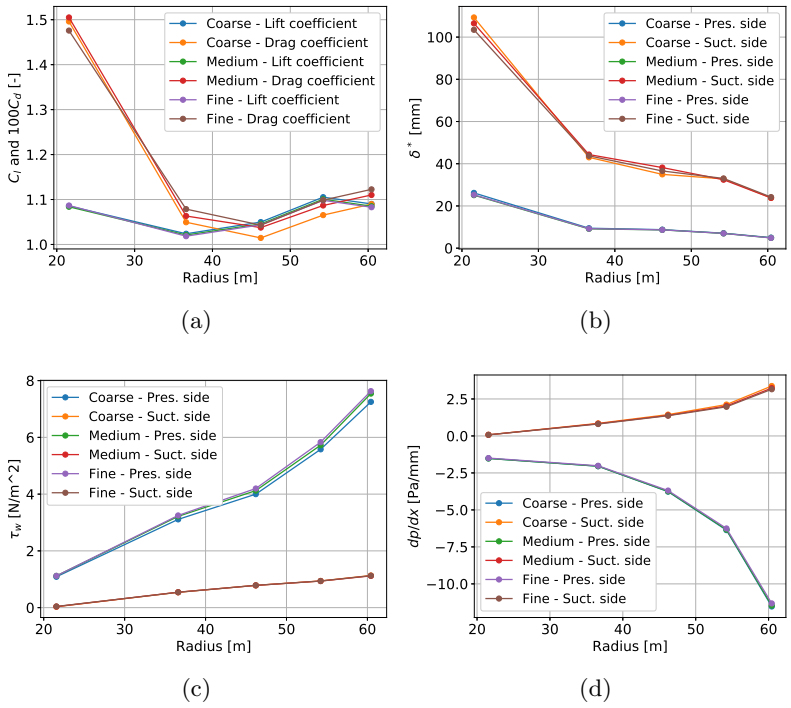

Figure 5: Mesh convergence study showing some parameters of interest as function of the radial position of the airfoil along the blade span for rated operating conditions. (a) Sectional lift and drag coefficients; (b) boundary layer displacement thickness; (c) wall shear stress; (d) pressure gradient. The boundary layer parameters have been extracted at 99% of the chord length.

addition to the lift and drag coefficients, the boundary layer parameters of interest for Amiet's theory are used as indicators for the mesh convergence study. The result shown in fig. 5 for the rated conditions highlights the weak dependence of the mesh utilized on the parameters of interest. Furthermore, for some of them, the values computed with the finer and coarser meshes are almost identical, suggesting a promising robustness with the mesh element size.

As an additional verification for the RANS simulation, the computed lift and drag coefficients are compared to the ones given in [7] and used for the BEMT simulations. Figure 6 compares the RANS results with the BEMT input for both the rigid and flexible rotor cases. The good agreement proves the consistency of the results within the workflow. In fig. 6a, a better agreement is noticed closer to the tip, where the 3D effects not considered in the 2D RANS are negligible. In the flexible rotor case the sectional lift coefficients are higher due to the pitchwise (torsional) deflection. The peak in the lift coefficient for the BEMT input is due to the high angle of attack of the airfoils close to the root and to 3D effects.

Finally, the dependency of the boundary layer parameters on the operating conditions has been used to check the consistency of the trends. As an example, fig. 7 shows the boundary layer displacement thickness for all the operating conditions tested. Up to the rated condition (11.4 m/s of wind speed) the boundary layer thickness on the suction side increases for almost all the blade sections. This is due to the increase in the angle of attack as the wind speed increases. In the above-rated condition (14 m/s wind speed), the pitch control decreases the angle of attack, reducing the boundary layer thicknesses for every blade segment.

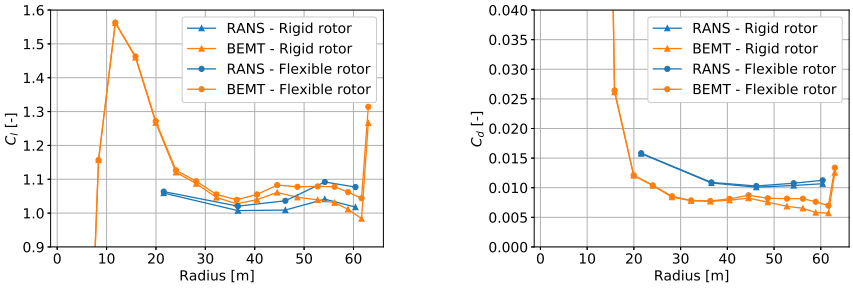

(a) (b)

Figure 6: Comparison between RANS results and BEMT input for (a) lift and (b) drag coefficients.

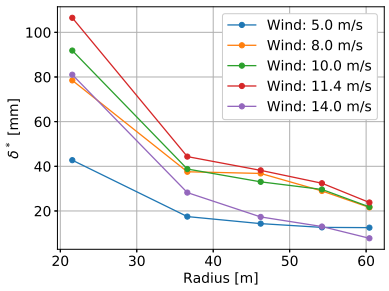

Figure 7: Boundary layer displacement thickness on the suction side of the airfoil for different operating conditions of the wind turbine.

3.3. Amiet's model validation

To the authors knowledge, acoustic measurements or accurate numerical simulations are not available for comparison in current literature. For this reason an in-depth analysis of the trends has been carried out for the simulations with both the rigid and flexible blades.

Figure 8a shows the overall A-weighted sound pressure level computed as

$$\mathrm{OASPL} = 10 \log_{10} \frac{\int_{f_1}^{f_2} S_{pp} \mathrm{d}f}{P_0^2}, \tag{3}$$

where $f_1 = 20$ Hz, $f_2 = 20000$ Hz, $P_0 = 2 \cdot 10^{-5}$ Pa and S_{pp} is the A-Weighted power spectral density, sum of the leading- and trailing-edge noise contributions. The power spectral density is computed for an observer located at ground level and 150 m downwind of the wind turbine. The OASPL is represented as a function of the power output computed with the BEMT. Each point on the curves represents an operative condition up to the rated condition. A qualitative comparison can be made with the work of Oerlemans and Schepers [8], where the same trends are reported, supported by experimental measurements.

Figure 8b shows the A-weighted sound pressure levels for the simulation with flexible blades in third-octave bands compared with the results of McBride and Burdisso [45]. In [45] the authors presented the results of NREL 5 MW wind turbine noise simulations using semi-empirical models coupled with an Hamiltonian ray tracing method for the atmospheric propagation. Several differences exist between the approach adopted in the reference [45] and in the present work and, hence, the results must be compared with caution. First, in the present work, the prediction does not include any atmospheric propagation model nor a wind speed gradient, differently

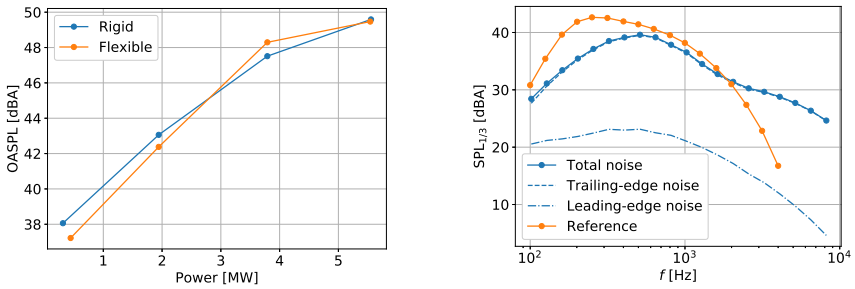

(a) (b)

Figure 8: Validation of Amiet's model. Observer located at ground level, 150 meters downwind. (a) Overall A-weighted sound pressure level. Each point represents a different operating condition up to the rated one. (b) Third octave, A-weighted sound pressure levels compared with results from reference [45] for a wind speed of 10 m/s.

from [45]. Furthermore, in [45], only the trailing-edge noise is computed using the BPM empirical model [46]. Nonetheless, in the mid-frequency range (400 Hz – 2.6 kHz), a satisfactory agreement with reference [45] is reported, while, significant deviations are observed in the low and high frequency ranges. The differences in the low frequency range can be attributed to the different trailing-edge noise models, since it is the main noise source for this test case: as shown in fig. 8b the leading-edge noise is several dB lower than the trailing-edge noise. The differences in the high-frequency range can be attributed to the atmospheric absorption which is expected to significantly affect the high-frequency far-field noise and it is not considered in the present work.

4. Results and discussion

4.1. Influence of the pitchwise and flapwise deflections

To assess the separate effect of the pitchwise and flapwise deflections, an additional acoustic simulation has been performed considering the pitchwise deflection only. The comparison between the noise predictions obtained considering rigid, pitchwise-flexible and fully-flexible blades is shown in fig. 9. The leading- and trailing-edge noise is computed at ground level up to a distance of 5 times the rotor radius. The rotor plane is the XZ plane and the wind is directed as the positive Y axis. Negligible differences are observed between the rigid (fig. 9a) and pitchwise-flexible simulations (fig. 9b), while the effect of the flapwise deflection (fig. 9c) is noticeable for observers close to the rotor plane: the shadow region is much less pronounced when the flapwise deflection is included, resulting in differences up to 13 dBA in the overall sound pressure level. On the contrary, negligible difference are observed in the upwind and downwind directions.

An important finding from the present study is that the symmetry with respect to the rotor plane is lost when the flapwise deflection is considered. For the rigid case the results are almost symmetric as shown, for example, in [8]. This is confirmed by the present work and shown in fig. 9a. On the contrary, the flapwise deflection introduces an asymmetry close to the rotor plane, as it can be observed in fig. 9c. This fact is more evident from the third-octave band analysis of the pressure shown in fig. 10 for the 1 kHz central frequency band. In fig. 10a the directivity pattern resulting from the simulation with rigid blades is symmetrical with respect to the rotor plane, while in fig. 10b higher noise levels are predicted in the downwind direction. The asymmetry is less pronounced for lower frequency bands.

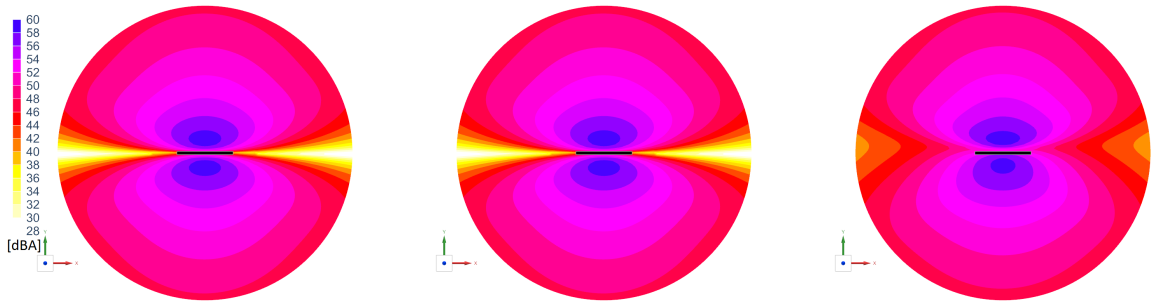

(a) (b) (c)

Figure 9: Footprint of the overall, A-weighted sound pressure level at rated conditions for the (a) rigid-blade simulation, (b) pitchwise-flexible blade simulation, and (c) fully-flexible blade simulation. The thick black line represents the rotor disk.

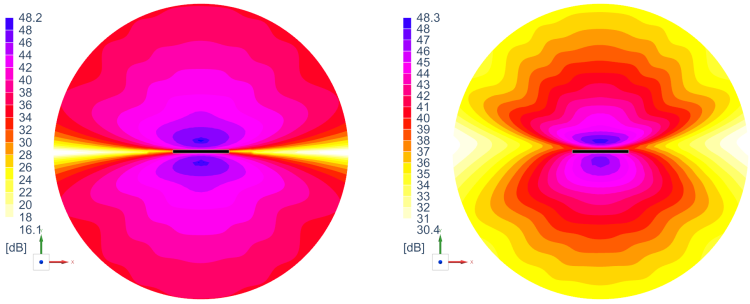

(a) (b)

Figure 10: Footprint of the third-octave pressure for the center frequency 1 kHz. (a) Rigid blades simulation; (b) fully-flexible blades simulation. Note that, differently form fig. 9, the scales are different to highlight the asymmetry in the noise footprints of the flexible blades.

4.2. Leading- and trailing-edge noise

For this wind turbine, the contribution of leading-edge noise to the total noise is negligible at low wind speed. Instead, for the rated and above-rated operating conditions, at low frequency, the leading edge noise becomes the dominant noise source. As an example, fig. 11a shows the A-weighted sound pressure levels for the above-rated conditions at ground level, 150 m downwind. At this observer position, the leading-edge noise becomes the dominant noise source below 100 Hz. This result is also supported by experimental studies from the literature, which state that the leading-edge becomes an important noise source at low frequency for large wind turbines [47]. It is worth mentioning that, even if A-weighted levels at low frequency are smaller than in the medium frequency range, the low frequency noise propagates more efficiently at large distances and, hence, the leading-edge low-frequency noise is expected to have more influence. In fig. 11b, the sound pressure level directivity is shown for the one-third octave band centered at 100 Hz to highlight that the leading edge noise contribution is particularly important in the downwind and crosswind directions.

5. Conclusions

The effect of blade deflections on the NREL wind turbine noise directivity is analysed by coupling the BEMT and a RANS-based Amiet's model. The numerical results show that, when the

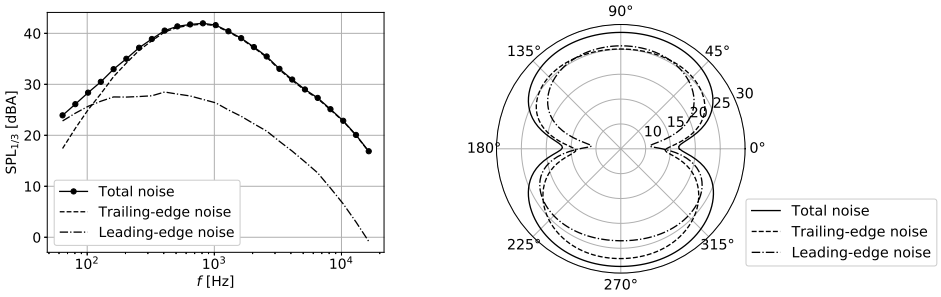

(a) (b)

Figure 11: Noise results obtained with flexible blades and above rated operating conditions. (a) A-weighted sound pressure levels at ground level, 150 m downwind; (b) directivity of the A-weighted sound pressure in [dBA] for the one-third octave center frequency 100 Hz, listeners at ground level and at a distance of 150 m, 90° corresponds to the downwind direction.

flapwise deflection is considered, the shadow region in the rotor plane is less pronounced: in particular, the overall sound pressure level increases in the crosswind direction up to 13 dBA. Furthermore, the symmetry of the results with respect to the rotor plane is lost when the flapwise deflection is included. For these reasons, the implementation of the blade deflections for the noise simulations should be considered for large wind turbines, which undergo significant blade deflections.

For the NREL 5-MW wind turbine considered in this work, the trailing-edge noise is the dominant noise source. The leading-edge noise contribution becomes significant only at high wind speed and low frequency. Furthermore, its contribution to the total noise is relevant in the downwind and crosswind directions.

Acknowledgements
The authors acknowledge the European Commission for its financial support through the H2020-MSCA-ITN-209 project zEPHYR (grant agreement No 860101).

References
[1] Imiela M and Wienke F 2015 Towards multidisciplinary wind turbine design using high-fidelity methods *33rd Wind Energy Symposium*
[2] Dose B, Rahimi H, Herráez I, Stoevesandt B and Peinke J 2018 *Renewable Energy* **129** 591–605
[3] Sayed M, Klein L, Lutz T and Krämer E 2019 *Renewable Energy* **140** 304–318
[4] Rinker J, Gaertner E, Zahle F, Skrzypiński W, Abbas N, Bredmose H, Barter G and Dykes K 2020 *Journal of Physics: Conference Series* **1618** 052052
[5] Kim H, Lee S, Son E, Lee S and Lee S 2012 *Renewable Energy* **42** 46–53
[6] Kaviani H R and Nejat A 2021 *Journal of Wind Engineering and Industrial Aerodynamics* **213** 104617
[7] Jonkman J, Butterfield S, Musial W and Scott G 2009 Definition of a 5-MW reference wind turbine for offshore system development Report National Renewable Energy Laboratory
[8] Oerlemans S and Schepers J G 2009 *International Journal of Aeroacoustics* **8** 555–584
[9] Amiet R K 1975 *Journal of Sound and Vibration* **41** 407 – 420
[10] Amiet R K 1976 *Journal of Sound and Vibration* **47** 387 – 393
[11] Küçükosman Y C, Christophe J and Schram C 2018 *Journal of Wind Engineering and Industrial Aerodynamics* **175** 305–IBC
[12] Küçükosman C 2019 *Semi-analytical approaches for the prediction of the noise produced by ducted wind turbines* Ph.D. thesis TU Delft University
[13] Siemens Digital Industries Software Siemens 2021 Simcenter 3D, version 2021.3

[14] Rozenberg Y, Roger M, Guédel A and Moreau S 2007 Rotating blade self noise: Experimental validation of analytical models *13th AIAA/CEAS Aeroacoustics Conference (28th AIAA Aeroacoustics Conference)*
[15] Tian Y and Cotté B 2016 *Acta Acustica united with Acustica* **102** 626–639
[16] Siemens Digital Industries Software Siemens 2021 Simcenter SAMCEF, version 2022.2
[17] Cardona A 1990 *An integrated approach to mechanism analysis* Thesis Liege University
[18] Hansen M O L, Sørensen J N, Voutsinas S, Sørensen N and Madsen H A 2006 *Progress in Aerospace Sciences* **42** 285–330
[19] Wang L, Liu X and Kolios A 2016 *Renewable and Sustainable Energy Reviews* **64** 195–210
[20] Glauert H 1935 *Airplane Propellers* (Berlin, Heidelberg: Springer Berlin Heidelberg) pp 169–360 ISBN 978-3-642-91487-4
[21] Burton T, Jenkins N, Sharpe D and Bossanyi E 2011 *Wind Energy Handbook* second edition ed (John Wiley and Sons)
[22] Prandtl L 1921 Applications of modern hydrodynamics to aeronautics NACA technical report No. 116
[23] Buhl M L 2005 A new empirical relationship between thrust coefficient and induction factor for the turbulent windmill state Report NREL
[24] Schlinker R H and Amiet R K 1981 Helicopter rotor trailing edge noise Tech. rep. National Aeronautics and Space Administration
[25] Roger M and Moreau S 2004 *AIAA Journal* **42** 536–544
[26] Moreau S and Roger M 2009 *Journal of Sound and Vibration* **323** 397 – 425
[27] Rozenberg Y, Roger M and Moreau S 2010 *AIAA Journal* **48** 951–962
[28] Kücükcoskun K, Christophe J, Schram C and Tournour M 2013 *International Journal of Aeroacoustics* **12** 85–104
[29] Kücükcoskun K, Christophe J and Schram C 2015 *FAN 2015 - International Conference on Fan Noise, Technology and Numerical Methods* **2015-April** 1–12
[30] Bertagnolio F, Madsen H A and Fischer A 2017 *Wind Energy* **20** 1331–1348
[31] Sinayoko S and Hurault J 2015 On predicting wind turbine noise and amplitude modulation using Amiet's theory *6th International Conference on Wind Turbine Noise* pp 1–15
[32] Roger M and Moreau S 2005 *Journal of Sound and Vibration* **286** 477 – 506
[33] Bresciani A P, Le Bras S and de Santana L D 2022 *Journal of Sound and Vibration* **524** 116742
[34] Corcos G M 1964 *Journal of Fluid Mechanics* **18** 353–378
[35] Goody M 2004 *AIAA Journal* **42** 1788–1794
[36] Rozenberg Y, Robert G and Moreau S 2012 *AIAA Journal* **50** 2168–2179
[37] Lee S 2018 *AIAA Journal* **56** 1818–1829
[38] Kamruzzaman M, Bekiropoulos D, Lutz T, Würz W and Krämer E 2015 *International Journal of Aeroacoustics* **14** 833–882
[39] Stalnov O, Chaitanya P and Joseph P F 2016 *Journal of Sound and Vibration* **372** 50–68
[40] Siemens Digital Industries Software Siemens 2021 Simcenter STAR-CCM+, version 2021.3
[41] Siemens Digital Industries Software Siemens 2021 Simcenter STAR-CCM+ User Guide v. 2021.1
[42] Counihan J 1975 *Atmospheric Environment (1967)* **9** 871–905
[43] Zhu W J, Heilskov N, Shen W Z and Sørensen J N 2005 *Journal of Solar Energy Engineering* **127** 517–528
[44] Sinayoko S, Kingan M J and Agarwal A 2013 *Proceedings of the Royal Society A: Mathematical, Physical and Engineering Sciences* **469**
[45] McBride S, Burdisso R and Parra J D 2016 *ICSV 2016 - 23rd International Congress on Sound and Vibration: From Ancient to Modern Acoustics*
[46] Brooks T F, Pope S D and Marcolini M A 1989 Airfoil self-noise and prediction Tech. rep. NASA, Langley Research Center
[47] Buck S, Oerlemans S and Palo S 2016 *Journal of Sound and Vibration* **385** 219–238